DEEPSPHERE: A GRAPH-BASED SPHERICAL CNN

Anonymous authors
Paper under double-blind review

ABSTRACT

Designing a convolution for a spherical neural network requires a delicate trade-off between efficiency and rotation equivariance. DeepSphere, a method based on a graph representation of the discretized sphere, strikes a controllable balance between these two desiderata. This contribution is twofold. First, we study both theoretically and empirically how equivariance is affected by the underlying graph with respect to the number of pixels and neighbors. Second, we evaluate DeepSphere on relevant problems. Experiments show state-of-the-art performance and demonstrates the efficiency and flexibility of this formulation. Perhaps surprisingly, comparison with previous work suggests that anisotropic filters might be an unnecessary price to pay.

1 INTRODUCTION

Spherical data is found in many applications (figure 1). Planetary data (such as meteorological or geological measurements) and brain activity are example of intrinsically spherical data. The observation of the universe, LIDAR scans, and the digitalization of 3D objects are examples of projections due to observation. Labels or variables are often to be inferred from them. Examples are the inference of cosmological parameters from the distribution of mass in the universe (Perraudin et al., 2019), the segmentation of omnidirectional images (Khasanova & Frossard, 2017), and the segmentation of cyclones from Earth observation (Mudigonda et al., 2017).

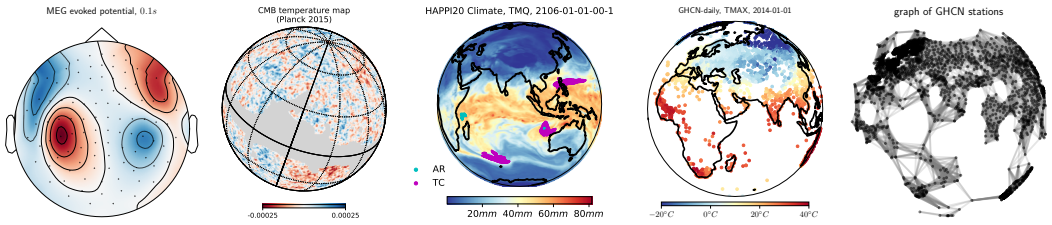

(a) (b) (c) (d) (e)

Figure 1: Examples of spherical data: (a) brain activity recorded through magnetoencephalography (MEG),[1](b) the cosmic microwave background (CMB) temperature from Planck Collaboration (2016), (c) hourly precipitation from a climate simulation (Jiang et al., 2019), (d) daily maximum temperature from the Global Historical Climatology Network (GHCN).[2]A rigid full-sphere pixelization is not ideal: brain activity is only measured on the scalp, the Milky Way's galactic plane masks observations, climate scientists desire a variable resolution, and the position of weather stations is arbitrary and changes over time. (e) Graphs can faithfully and efficiently represent sampled spherical data by placing vertices where it matters.

As neural networks (NNs) have proved to be great tools for inference, variants have been developed to handle spherical data. Exploiting the locally Euclidean property of the sphere, early attempts used standard 2D convolutions on a grid discretization of the sphere (Boomsma & Frellsen, 2017; Su & Grauman, 2017; Coors et al., 2018). While simple and efficient, those convolutions are not equivariant to rotations. On the other side of this tradeoff, Cohen et al. (2018) and Esteves et al.

[1] https://martinos.org/mne/stable/auto_tutorials/plot_visualize_evoked.html
[2] https://www.ncdc.noaa.gov/ghcn-daily-description

(2018) proposed to perform proper spherical convolutions through the spherical harmonic transform. While equivariant to rotations, those convolutions are expensive (section 2).

As a lack of equivariance can penalize performance (section 4.2) and expensive convolutions prohibit their application to some real-world problems, methods standing between these two extremes are desired. Cohen et al. (2019) proposed to reduce costs by limiting the size of the representation of the symmetry group by projecting the data from the sphere to the icosahedron. The distortions introduced by this projection might however hinder performance (section 4.3).

Another approach is to represent the discretized sphere as a graph connecting pixels according to the distance between them (Bruna et al., 2013; Khasanova & Frossard, 2017; Perraudin et al., 2019). While Laplacian-based graph convolutions are more efficient than spherical convolutions, they are not exactly equivariant (Defferrard et al., 2019). In this work, we argue that graph-based spherical CNNs strike an interesting balance, with a controllable tradeoff between cost and equivariance (which is linked to performance). Experiments on multiple problems of practical interest show the competitiveness and flexibility of this approach.

2 METHOD

DeepSphere leverages graph convolutions to achieve the following properties: (i) computational efficiency, (ii) sampling flexibility, and (iii) rotation equivariance (section 3). The main idea is to model the discretized sphere as a graph of connected pixels: the length of the shortest path between two pixels is an approximation of the geodesic distance between them. We use the graph CNN formulation introduced in (Defferrard et al., 2016) and a pooling strategy that exploits hierarchical pixelizations of the sphere.

Sampling. Given a sampling scheme $\mathcal{V} = \{x_i \in \mathbb{S}^2\}_{i=1}^n$, a function $f : \mathbb{S}^2 \supset F_\mathcal{V} \to \mathbb{R}$ is sampled as $T_\mathcal{V}(f) = \boldsymbol{f}$ by the sampling operator $T_\mathcal{V} : L^2(\mathbb{S}^2) \supset F_\mathcal{V} \to \mathbb{R}^n$ defined as $\boldsymbol{f} : f_i = f(x_i)$, where $F_\mathcal{V}$ will be specified in section 3. As there is no analogue of uniform sampling on the sphere, many schemes have been proposed with different tradeoffs. In this work, depending on the considered application, we will use the equiangular (Driscoll & Healy, 1994), HEALPix (Gorski et al., 2005), and icosahedral (Baumgardner & Frederickson, 1985) grids.

Graph. From $\mathcal{V}$, we construct a weighted undirected graph $\mathcal{G} = (\mathcal{V}, w)$, where the elements of $\mathcal{V}$ are the vertices and the weight $w_{ij} = w_{ji}$ is a similarity measure between vertices x_i and x_j. The combinatorial graph Laplacian $\boldsymbol{L} \in \mathbb{R}^{n \times n}$ is defined as $\boldsymbol{L} = \boldsymbol{D} - \boldsymbol{A}$, where $\boldsymbol{A} = (w_{ij})$ is the weighted adjacency matrix, $\boldsymbol{D} = (d_{ii})$ is the diagonal degree matrix, and $d_{ii} = \sum_j w_{ij}$ is the weighted degree of vertex x_i. Given a sampling scheme $\mathcal{V}$, usually fixed by the application or the available measurements, the freedom in constructing $\mathcal{G}$ is in setting w. Section 3 shows how to set w to minimize the equivariance error.

Convolution. On Euclidean domains, convolutions are efficiently implemented by sliding a window in the signal domain. On the sphere however, there is no straightforward way to implement a convolution in the signal domain due to non-uniform samplings. Convolutions are most often performed in the spectral domain through a spherical harmonic transform (SHT). That is the approach taken by Cohen et al. (2018) and Esteves et al. (2018), which has a computational cost of $\mathcal{O}(n^{3/2})$ on isolatitude pixelizations (such as the HEALPix and equiangular grids) and $\mathcal{O}(n^2)$ in general. On the other hand, following Defferrard et al. (2016), graph convolutions can be defined as

$$h(\boldsymbol{L})\boldsymbol{f} = \left(\sum_{i=0}^{K} \alpha_i \boldsymbol{L}^i \right) \boldsymbol{f}, \tag{1}$$

where K is the polynomial order (which corresponds to the filter's size) and α_i are the coefficients to be optimized during training.[3] Those convolutions are used by Khasanova & Frossard (2017) and Perraudin et al. (2019) and cost $\mathcal{O}(n)$ operations through a recursive application of $\boldsymbol{L}$.[4]

[3] In practice, training with Chebyshev polynomials (instead of monomials) is slightly more stable. We believe it to be due to their orthogonality and uniformity.

[4] As long as the graph is sparsified such that the number of edges, i.e., the number of non-zeros in $\boldsymbol{A}$, is proportional to the number of vertices n. This can always be done as most weights are very small.

Pooling. Down- and up-sampling is natural for hierarchical pixelizations,[5] where each subdivision divides a pixel in (an equal number of) child sub-pixels. To pool (down-sample), the data supported on the sub-pixels is summarized by a permutation invariant function such as the maximum or the average. To unpool (up-sample), the data supported on a pixel is copied to all its sub-pixels.

Architecture. All our NNs are fully convolutional, and employ a global average pooling (GAP) for rotation invariant tasks. Graph convolutional layers are always followed by batch normalization and ReLU activation, except in the last layer. Note that batch normalization and activation act on the elements of $\boldsymbol{f}$ independently, and hence don't depend on the domain of f.

3 GRAPH CONVOLUTION AND EQUIVARIANCE

While the graph framework offers great flexibility, its ability to faithfully represent the underlying sphere — for graph convolutions to be rotation equivariant — highly depends on the sampling locations and the graph construction.

3.1 PROBLEM FORMULATION

We require $F_{\mathcal{V}}$ to be a suitable subspace of $L^2(\mathbb{S}^2)$ such that $T_{\mathcal{V}}$ is invertible, i.e., the function $f \in F_{\mathcal{V}}$ can be unambiguously reconstructed from its sampled values $\boldsymbol{f}$. The existence of such a subspace depends on the sampling scheme $\mathcal{V}$, and its characterization is a common problem in signal processing (Driscoll & Healy, 1994). For most sampling schemes, it is not known if $F_{\mathcal{V}}$ exists and hence if $T_{\mathcal{V}}$ is invertible. A special case is the equiangular sampling scheme where a sampling theorem holds, and thus a closed form of $T_{\mathcal{V}}^{-1}$ is known. For sampling schemes where no such sampling formula is available, we leverage the discrete SHT to reconstruct f from $\boldsymbol{f} = T_{\mathcal{V}} f$, thus approximating $T_{\mathcal{V}}^{-1}$. For all theoretical considerations, we assume that $F_{\mathcal{V}}$ exists and $f \in F_{\mathcal{V}}$.

By definition, the (spherical) graph convolution is rotation equivariant, if and only if, it commutes with the rotation operator defined as $R(g), g \in SO(3)$: $R(g)f(x) = f\left(g^{-1}x\right)$. In the context of this work, graph convolution is performed by recursive applications of the graph Laplacian (equation (1)). Hence, if $\boldsymbol{L}$ commutes with the rotation operator, then, by recursion, it will also commute with the convolution $h(\boldsymbol{L})$. As a result, to simplify our analysis, we concentrate on the graph Laplacian and $h(\boldsymbol{L})$ is rotational invariant if and only if

$$\boldsymbol{R}_{\mathcal{V}}(g)\boldsymbol{L}\boldsymbol{f} = \boldsymbol{L}\boldsymbol{R}_{\mathcal{V}}(g)\boldsymbol{f} \qquad \forall f \in F_{\mathcal{V}} \text{ and } \forall g \in SO(3), \tag{2}$$

where $\boldsymbol{R}_{\mathcal{V}}(g) = T_{\mathcal{V}} R(g) T_{\mathcal{V}}^{-1}$. For practical a evaluation of the equivariance, we define the *normalized equivariance error* for a signal $\boldsymbol{f}$, and a rotation g as:

$$E_{\boldsymbol{L}}(\boldsymbol{f}, g) = \left(\frac{\|\boldsymbol{R}_{\mathcal{V}}(g)\boldsymbol{L}\boldsymbol{f} - \boldsymbol{L}\boldsymbol{R}_{\mathcal{V}}(g)\boldsymbol{f}\|}{\|\boldsymbol{L}\boldsymbol{f}\|} \right)^2, \tag{3}$$

More generally for a class of signal $f \in C \subset F_{\mathcal{V}}$, the *mean equivariance error* defined as

$$\overline{E}_{\boldsymbol{L},C} = \mathbb{E}_{\boldsymbol{f} \in C, g \in SO(3)} \, E_{\boldsymbol{L}}(\boldsymbol{f}, g), \tag{4}$$

represents well the overall equivariance error. In practice, we analyse this error with respect of the frequency by setting the set C to functions f made of single degree spherical harmonic. The expected value is obtained by averaging over a finite number of random functions and random rotations.

3.2 FINDING THE OPTIMAL SET OF WEIGHTS

Naturally, Khasanova & Frossard (2017) designed a Laplacian $\boldsymbol{L}$ that minimizes (3) for specific rotations on the longitude and latitude axis. Working specifically with the equiangular sampling, they consider the set $\mathcal{G}$ of all the possible graphs where each node is connected only to four of its nearest neighbours (North, South, West, East). Their approach leads to weights w_{ij} inversely proportional to the Euclidean distance between vertices:

$$w_{ij} = \frac{1}{\|x_i - x_j\|} \tag{5}$$

[5] The equiangular, HEALPix, and icosahedral schemes are of this kind.

We chose a different approach and take inspiration from Belkin & Niyogi (2008), which proves that for a random *uniform sampling* scheme the graph Laplacian converges toward the Laplace-Beltrami operator $\Delta_{\mathbb{S}^2}$ as the number of sampling points goes to infinity. This convergence result is important as a) $\Delta_{\mathbb{S}^2}$ commutes with rotation ($\Delta_{\mathbb{S}^2} R(g) = R(g)\Delta_{\mathbb{S}^2}$) and b) is diagonalized by the spherical harmonics. In this case the weighting scheme is full (every node is connected to every node) and is based on the exponential kernel:

$$w_{ij} = e^{-\frac{1}{4t}\|x_i - x_j\|^2} \tag{6}$$

In practice, because of the exponential, most of the weights are very close to 0. Hence, to optimize for computational efficiency, we limit ourselves to only the k nearest neighbors. Given k, the optimal t is found by searching for the minimizer of (4). Figure 3 shows the optimal kernel widths found for various resolutions of the HEALPix grid.

3.3 Analysis of the proposed weighting scheme

We analyse our proposed weighting scheme both theoretically and empirically.

Theoretical convergence. We extend the work of Belkin and Nyiogi to a sufficiently regular, deterministic sampling scheme. Given a sampling scheme $\mathcal{V} = \{x_0, \dots, x_{n-1}\}$, define σ_i to be the patch of the surface of the sphere corresponding to x_i, A_i its corresponding area and d_i the radius of the smallest ball in $\mathbb{R}^3$ containing σ_i. Define $d^{(n)} := \max_{i=0,\dots,n} d_i$ and $A^{(n)} = \max_{i=0,\dots,n} A_i$.

Theorem 3.1. *For a sampling $\mathcal{V} = \{x_i \in \mathbb{S}^2\}_{i=0}^{n-1}$ of the sphere that is equi-area and such that $d^{(n)} \leq \frac{C}{\alpha},\ \alpha \in (0, 1/2]$, for all $f : \mathbb{S}^2 \to \mathbb{R}$ Lipschitz with respect to the Euclidean distance in $\mathbb{R}^3$, for all $y \in \mathbb{S}^2$, there exists a sequence $t_n = n^\beta$ such that*

$$\lim_{n\to\infty} \frac{|\mathbb{S}^2|}{4\pi t_n^2} \boldsymbol{L}_n^{t_n} T_{\mathcal{V}} f[i] = \Delta_{\mathbb{S}^2} f(x_i) \quad \forall i = 0, ..., n-1.$$

As a direct implication of this theorem, $\boldsymbol{L}$ converges pointwisely toward the Laplace-Beltrami operator ($\Delta_{\mathbb{S}^2}$). This operator commutes with rotation and hence this convergence is a strong hint for equivariance. Importantly, the proof of Theorem 3.1 in Appendix A inspires us in the construction of our graph Laplacian. It is inspirational for the graph construction and for how the parameter t needs to be adjusted with respect to the number of points n.

Nevetheless, it is important to keep in mind the limits of Theorem 3.1. First, it is *not* a proof of equivariance of the graph convolution for a specific sampling. To construct such a proof, a stronger convergence result is needed, for example uniform convergence (instead of pointwise). We note that in the random sampling case, the graph laplacian does *not* converges uniformly in general (Belkin & Niyogi, 2007, Sec. 3), but does for a class of Lipschitz functions (Belkin & Niyogi, 2008, Sec. 6). Second, while do not have a formal proof for it, we strongly believe that the HEALPix sampling does satisfy the hypothesis $d^{(n)} \leq \frac{C}{n^\alpha},\ \alpha \in (0, 1/2]$ with α very close or equal to $1/2$. The empirical results discussed in the next paragraph also point in this direction. This is further discussed in Appendix A.

Empirical convergence. In figure 2, we present the equivariance error $\bar{E}_{\boldsymbol{L},C(\ell)}$ (4) computed numerically as a function of the frequency (degree) ℓ, for different parameter sets of DeepSphere as well as for graph construction of Khasanova & Frossard (2017). The error depends of the number of pixels: $12N_{side}^2$ for HEALPix and $4b^2$ for the equiangular sampling. Here N_{side} and b are the sampling parameters determining their precision. The frequencies ℓ of the monochromatic signals were chosen in the range $(0,\ 3N_{side} - 1)$ for the Healpix sampling, and in the range $(0, b)$ for the equiangular sampling, to allow for an almost perfect implementation (up to numerical errors) of the operator $\boldsymbol{R}_{\mathcal{V}}$ in equation (4) (Gorski et al., 1999). Using these parameters, the error measured is mostly due to imperfections in the empirical approximation of the Laplace-Beltrami operator and not to the sampling.

For 8 neighbors, selecting the optimal value of t already leads to an improvement compared to Perraudin et al. (2019), whose graph also was constructed to have at maximum 8 neighbors. With higher the number of neighbors, the equivariance error decreases by more than one order of magnitude. Furthermore, increasing the graph resolution (N_{side}) leads to an improvement in the high frequencies as

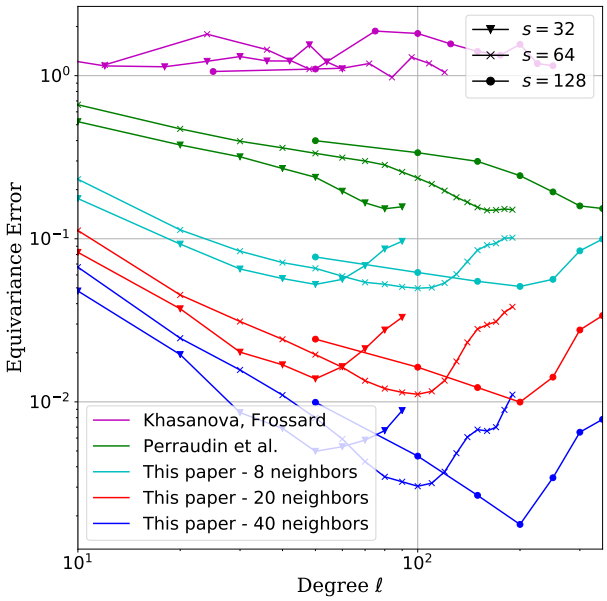

Figure 2: Normalized mean equivariance error (4). The number of pixels is $4s^2$ for the equiangular sampling and $12s^2$ for the Healpix sampling.

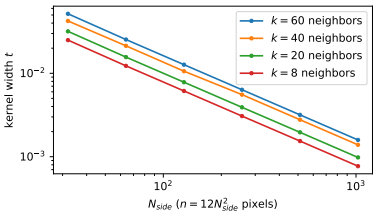

Figure 3: Optimal kernel widths.

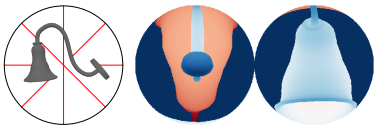

Figure 4: 3D object represented as a spherical depth map.

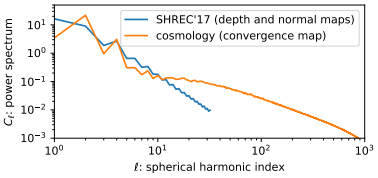

Figure 5: Power spectral densities.

well. Increasing the graph resolution of the graph of Khasanova & Frossard (2017) does not seem to improve its equivariance. We note that in our numerical test, this graph was perfectly equivariant to rotations along the horizontal and vertical axis as it should be by design. Nevertheless, it is simply not equivariant along the last rotation. Such equivariance properties might be sufficient for analysing omnidirectional images (that are naturally aligned on the north-south axis).

4 Experiments

4.1 3D objects recognition

The recognition of 3D shapes is a rotation invariant task: rotating an object doesn't change its nature. While 3D shapes are usually represented as meshes or point clouds, representing them as spherical maps (figure 4) naturally allows a rotation invariant treatment.

The SHREC'17 shape retrieval contest (Savva et al., 2017) contains 51,300 randomly oriented 3D models from ShapeNet (Chang et al., 2015), to be classified in 55 categories (tables, lamps, airplanes, etc.). As in Cohen et al. (2018), objects are represented by 6 spherical maps. At each pixel, a ray is traced towards the center of the sphere. The distance from the sphere to the object forms a depth map. The $\cos$ and $\sin$ of the surface angle forms two normal maps. The same is done for the object's convex hull.[6] The maps are discretized using either an equiangular grid with bandwidth $b = 64$ ($n = 4b^2 = 16,384$ pixels) or an HEALPix grid with $N_{side} = 32$ ($n = 12N_{side}^2 = 12,288$ pixels).

The equiangular graph is built with equation (5) and $k = 4$ neighbors (following Khasanova & Frossard, 2017). The HEALPix graph is built with equation (6), $k = 8$, and a kernel width t set to the average of the distances (following Perraudin et al., 2019). The NN is made of 5 graph convolutional layers, each followed by a max pooling layer which down-samples by 4. A GAP and a fully connected layer with softmax follow. The polynomials are all of order $K = 3$ and the number of channels per layer is $16, 32, 64, 128, 256$, respectively. Following Esteves et al. (2018), the cross-entropy plus a triplet loss is optimized with Adam for 30 epochs on the dataset augmented by 3 random translations. The learning rate is $5 \cdot 10^{-2}$ and the batch size is 32.

[6] Albeit we didn't observe much improvement by using the convex hull.

	performance		size	speed	
	F1	mAP	params	inference	training
Cohen et al. (2018) ($b = 128$)	-	67.6	1400 k	38.0 ms	50 h
Cohen et al. (2018) (simplified,[7] $b = 64$)	78.9	66.5	400 k	12.0 ms	32 h
Esteves et al. (2018) ($b = 64$)	79.4	68.5	500 k	9.8 ms	3 h
DeepSphere (equiangular $b = 64$)	79.4	66.5	190 k	0.9 ms	50 m
DeepSphere (HEALPix $N_{side} = 32$)	80.7	68.6	190 k	0.9 ms	50 m

Table 1: Results on SHREC'17 (3D shapes). DeepSphere achieves similar performance at a much lower cost, suggesting that anisotropic filters are an unnecessary price to pay.

	accuracy	time
Perraudin et al. (2019), 2D CNN baseline	54.2	104 ms
Perraudin et al. (2019), CNN variant, $k = 8$	62.1	185 ms
Perraudin et al. (2019), FCN variant, $k = 8$	83.8	185 ms
$k = 8$ neighbors, t from section 3.2	87.1	185 ms
$k = 20$ neighbors, t from section 3.2	91.3	250 ms
$k = 40$ neighbors, t from section 3.2	92.5	363 ms

Table 2: Results on the classification of partial convergence maps. Lower equivariance error translates to higher performance.

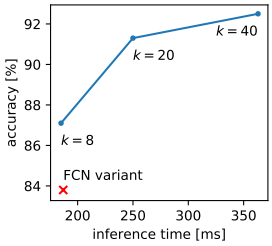

Figure 6: Tradeoff between cost and accuracy.

Results are shown in table 1. As the network is trained for shape classification rather than retrieval, we report the classification F1 alongside the mAP used in the retrieval contest.[8] DeepSphere achieves the same performance as Cohen et al. (2018) and Esteves et al. (2018) at a much lower cost, suggesting that anisotropic filters are an unnecessary price to pay. As the information in those spherical maps resides in the low frequencies (figure 5), reducing the equivariance error didn't translate into improved performance. For the same reason, using the more uniform HEALPix discretization or lowering the resolution down to $N_{side} = 8$ ($n = 768$ pixels) didn't impact performance either.

4.2 Cosmological model classification

Given observations, cosmologists estimate the posterior probability of cosmological parameters, such as the matter density Ω_m and the normalization of the matter power spectrum σ_8. Those parameters are typically estimated by likelihood-free inference, which requires a function to predict the parameters from simulations. As that is complicated to setup, prediction methods are typically benchmarked on the classification of spherical maps instead (Schmelzle et al., 2017). We used the same task, data, and setup as Perraudin et al. (2019): the classification of 720 partial convergence maps made of $n \approx 10^6$ pixels ($1/12 \approx 8\%$ of a sphere at $N_{side} = 1024$) from two ΛCDM cosmological models, ($\Omega_m = 0.31$, $\sigma_8 = 0.82$) and ($\Omega_m = 0.26$, $\sigma_8 = 0.91$), at a relative noise level of 3.5 (i.e., the signal is hidden in noise of 3.5 times higher standard deviation). Convergence maps represent the distribution of over- and under-densities of mass in the universe (see Bartelmann, 2010, for a review of gravitational lensing).

Graphs are built with equation (6), $k = 8, 20, 40$ neighbors, and the corresponding optimal kernel widths t given in section 3.2. Following Perraudin et al. (2019), the NN is made of 5 graph convolutional layers, each followed by a max pooling layer which down-samples by 4. A GAP and a fully connected layer with softmax follow. The polynomials are all of order $K = 4$ and the number of channels per layer is $16, 32, 64, 64, 64$, respectively. The cross-entropy loss is optimized with Adam for 80 epochs. The learning rate is $2 \cdot 10^{-4} \cdot 0.999^{\text{step}}$ and the batch size is 8.

Unlike on SHREC'17, results (table 2) show that a lower equivariance error on the convolutions translates to higher performance. That is probably due to the high frequency content of those maps (figure 5). There is a clear cost-accuracy tradeoff, controlled by the number of neighbors k (figure 6).

[5] As implemented in `https://github.com/jonas-koehler/s2cnn`.

[8] We omit the F1 for Cohen et al. (2018) as we didn't get the mAP reported in the paper when running it.

	accuracy	mAP
Jiang et al. (2019) (rerun)	94.95	38.41
Cohen et al. (2019) (S2R)	97.5	68.6
Cohen et al. (2019) (R2R)	97.7	75.9
DeepSphere (weighted loss)	97.8 ± 0.3	77.15 ± 1.94
DeepSphere (non-weighted loss)	87.8 ± 0.5	89.16 ± 1.37

Table 3: Results on climate event segmentation: mean accuracy (over TC, AR, BG) and mean average precision (over TC and AR). DeepSphere achieves state-of-the-art performance.

This experiment moreover demonstrates DeepSphere's flexibility (using partial spherical maps) and scalability (competing spherical CNNs were tested on maps of at most $10,000$ pixels).

4.3 Climate event segmentation

We evaluate our method on a task proposed by (Mudigonda et al., 2017): the segmentation of extreme climate events, Tropical Cyclones (TC) and Atmospheric Rivers (AR), in global climate simulations (figure 1c). The data was produced by a 20-year run of the Community Atmospheric Model v5 (CAM5) and consists of 16 channels such as temperature, wind, humidity, and pressure at multiple altitudes. We used the pre-processed dataset from (Jiang et al., 2019).[9] There is 1,072,805 spherical maps, down-sampled to a level-5 icosahedral grid ($n = 10 \cdot 4^l + 2 = 10,242$ pixels). The labels are heavily unbalanced with 0.1% TC, 2.2% AR, and 97.7% background (BG) pixels.

The graph is built with equation (6), $k = 6$ neighbors, and a kernel width t set to the average of the distances. Following Jiang et al. (2019), the NN is an encoder-decoder with skip connections. Details in section B.3. The polynomials are all of order $K = 3$. The cross-entropy loss (weighted or non-weighted) is optimized with Adam for 30 epochs. The learning rate is $1 \cdot 10{-}3$ and the batch size is 64.

Results are shown in table 3 (details in tables 6, 7 and 8). The mean and standard deviation are computed over 5 runs. Note that while Jiang et al. (2019) and Cohen et al. (2019) use a weighted cross-entropy loss, that is a suboptimal proxy for the mAP metric. DeepSphere achieves state-of-the-art performance, suggesting again that anisotropic filters are unnecessary. Note that results from Mudigonda et al. (2017) cannot be directly compared as they don't use the same input channels.

Compared to Cohen et al. (2019)'s conclusion, it is surprising that S2R does worse than DeepSphere (which is limited to S2S). Potential explanations are (i) that their icosahedral projection introduces harmful distortions, or (ii) that a larger architecture can compensate for the lack of generality. We indeed observed that more feature maps and depth led to higher performance (section B.3).

4.4 Uneven sampling

To demonstrate the flexibility of modeling the discretized sphere by a graph, we collected historical measurements from $n \approx 10,000$ weather stations scattered across the Earth.[10] The spherical data is heavily non-uniformly sampled, with a much higher density of weather stations over North America than the Pacific (figure 1d). For illustration, we devised two artificial tasks. A dense regression: predict the temperature on a given day knowing the temperature on the previous 5 days. A global regression: predict the day (represented as one period of a sine over the year) from temperature or precipitations. Predicting from temperature is much easier as it has a clear yearly pattern.

The graph is built with equation (6), $k = 5$ neighbors, and a kernel width t set to the average of the distances. The equivariance property of the resulting graph has not been tested, and we don't expect it to be good due to the heavily non-uniform sampling. The NN is made of 3 graph convolutional layers. The polynomials are all of order $K = 0$ or 4 and the number of channels per layer is $50, 100, 100$, respectively. For the global regression, a GAP and a fully connected layer follow. For

[9] Available at `http://island.me.berkeley.edu/ugscnn/data`.

[10] `https://www.ncdc.noaa.gov/ghcn-daily-description`

	temp. (from past temp.)			day (from temperature)			day (from precipitations)		
order K	MSE	MAE	R2	MSE	MAE	R2	MSE	MAE	R2
0	10.88	2.42	0.896	0.10	0.10	0.882	0.58	0.42	-0.980
4	8.20	2.11	0.919	0.05	0.05	0.969	0.50	0.18	0.597

Table 4: Prediction results on data from weather stations. Structure always improves performance.

the dense regression, a graph convolutional layer follows instead. The MSE loss is optimized with RMSprop for 250 epochs. The learning rate is $1 \cdot 10^{-3}$ and the batch size is 64.

Results are shown in table 4. While using a polynomial order $K = 0$ is like modeling each time series independently with an MLP, orders $K > 0$ integrate neighborhood information. Results show that using the structure induced by the spherical geometry always yields better performance.

5 Conclusion

This work showed that DeepSphere strikes an interesting, and we think currently optimal, balance between desiderata for a spherical CNN. A single parameter, the number of neighbors k a pixel is connected to in the graph, controls the tradeoff between cost and equivariance (which is linked to performance). As computational cost and memory consumption scales linearly with the number of pixels, DeepSphere scales to spherical maps made of millions of pixels, a required resolution to faithfully represent cosmological and climate data. Also relevant in scientific applications is the flexibility offered by a graph representation (for partial coverage, missing data, and non-uniform samplings). Finally, the implementation of the graph convolution is straightforward, and the ubiquity of graph neural networks — pushing for their first-class support in DL frameworks — will make implementations even easier and more efficient.

A potential drawback of graph Laplacian-based approaches is the isotropy of graph filters, reducing in principle the expressive power of the NN. Experiments from Cohen et al. (2019) and Boscaini et al. (2016) indeed suggest that more general convolutions achieve better performance. Our experiments on 3D shapes (section 4.1) and climate (section 4.3) however show that DeepSphere's isotropic filters do not hinder performance. Possible explanations for this discrepancy are that NNs somehow compensate for the lack of anisotropic filters, or that some tasks can be solved with isotropic filters. The distortions induced by the icosahedral projection in Cohen et al. (2019) or the leakage of curvature information in Boscaini et al. (2016) might also alter performance.

Developing graph convolutions on irregular samplings that respect the geometry of the sphere is another research direction of importance. Practitioners currently interpolate their measurements (coming from arbitrarily positioned weather stations, satellites or telescopes) to regular samplings. This practice either results in a waste of precision or computational and storage resources. Our ultimate goal is for practitioners to be able to work directly on their measurements, however distributed.

AUTHOR CONTRIBUTIONS

Left blank for anonymity reason.

ACKNOWLEDGMENTS

Left blank for anonymity reason.

REFERENCES

M. Bartelmann. Gravitational lensing. *Classical and Quantum Gravity*, 2010.

John R Baumgardner and Paul O Frederickson. Icosahedral discretization of the two-sphere. *SIAM Journal on Numerical Analysis*, 1985.

Mikhail Belkin and Partha Niyogi. Convergence of laplacian eigenmaps. In *Advances in Neural Information Processing Systems*, 2007.

Mikhail Belkin and Partha Niyogi. Towards a theoretical foundation for laplacian-based manifold methods. *Journal of Computer and System Sciences*, 2008.

Wouter Boomsma and Jes Frellsen. Spherical convolutions and their application in molecular modelling. In *Advances in Neural Information Processing Systems*, 2017.

Davide Boscaini, Jonathan Masci, Emanuele Rodolà, and Michael Bronstein. Learning shape correspondence with anisotropic convolutional neural networks. In *Advances in Neural Information Processing Systems*, 2016.

Joan Bruna, Wojciech Zaremba, Arthur Szlam, and Yann LeCun. Spectral networks and locally connected networks on graphs. *arXiv:1312.6203*, 2013. URL https://arxiv.org/abs/1312.6203.

Angel X Chang, Thomas Funkhouser, Leonidas Guibas, Pat Hanrahan, Qixing Huang, Zimo Li, Silvio Savarese, Manolis Savva, Shuran Song, Hao Su, et al. Shapenet: An information-rich 3d model repository. *arXiv:1512.03012*, 2015.

Taco S Cohen, Mario Geiger, Jonas Koehler, and Max Welling. Spherical cnns. In *International Conference on Learning Representations (ICLR)*, 2018. URL https://arxiv.org/abs/1801.10130.

Taco S. Cohen, Maurice Weiler, Berkay Kicanaoglu, and Max Welling. Gauge equivariant convolutional networks and the icosahedral cnn. In *International Conference on Machine Learning (ICML)*, 2019. URL http://arxiv.org/abs/1902.04615.

Benjamin Coors, Alexandru Paul Condurache, and Andreas Geiger. Spherenet: Learning spherical representations for detection and classification in omnidirectional images. In *European Conference on Computer Vision*, 2018.

Michaël Defferrard, Xavier Bresson, and Pierre Vandergheynst. Convolutional neural networks on graphs with fast localized spectral filtering. In *Advances in Neural Information Processing Systems*, 2016. URL https://arxiv.org/abs/1606.09375.

Michaël Defferrard, Nathanaël Perraudin, Tomasz Kacprzak, and Raphael Sgier. Deepsphere: towards an equivariant graph-based spherical cnn. In *ICLR Workshop on Representation Learning on Graphs and Manifolds*, 2019. URL https://arxiv.org/abs/1904.05146.

J. R. Driscoll and D. M. Healy. Computing fourier transforms and convolutions on the 2-sphere. *Adv. Appl. Math.*, 1994. URL http://dx.doi.org/10.1006/aama.1994.1008.

Carlos Esteves, Christine Allen-Blanchette, Ameesh Makadia, and Kostas Daniilidis. Learning so(3) equivariant representations with spherical cnns. In *Proceedings of the European Conference on Computer Vision (ECCV)*, 2018. URL https://arxiv.org/abs/1711.06721.

Krzysztof M Gorski, Benjamin D Wandelt, Frode K Hansen, Eric Hivon, and Anthony J Banday. The healpix primer. *arXiv preprint astro-ph/9905275*, 1999.

Krzysztof M Gorski, Eric Hivon, AJ Banday, Benjamin D Wandelt, Frode K Hansen, Mstvos Reinecke, and Matthia Bartelmann. Healpix: a framework for high-resolution discretization and fast analysis of data distributed on the sphere. *The Astrophysical Journal*, 2005.

Chiyu "Max" Jiang, Jingwei Huang, Karthik Kashinath, Prabhat, Philip Marcus, and Matthias Niessner. Spherical cnns on unstructured grids. In *International Conference on Learning Representations (ICLR)*, 2019. URL https://arxiv.org/abs/1901.02039.

Renata Khasanova and Pascal Frossard. Graph-based classification of omnidirectional images. In *Proceedings of the IEEE International Conference on Computer Vision*, 2017. URL https://arxiv.org/abs/1707.08301.

Mayur Mudigonda, Sookyung Kim, Ankur Mahesh, Samira Kahou, Karthik Kashinath, Dean Williams, Vincen Michalski, Travis OBrien, and Mr Prabhat. Segmenting and tracking extreme climate events using neural networks. In *Deep Learning for Physical Sciences (DLPS) Workshop, held with NIPS Conference*, 2017. URL https://dl4physicalsciences.github.io/files/nips_dlps_2017_20.pdf.

Nathanaël Perraudin, Michaël Defferrard, Tomasz Kacprzak, and Raphael Sgier. Deepsphere: Efficient spherical convolutional neural network with healpix sampling for cosmological applications. *Astronomy and Computing*, 2019. URL https://arxiv.org/abs/1810.12186.

Planck Collaboration. Planck 2015 results. i. overview of products and scientific results. *Astronomy & Astrophysics*, 2016.

Manolis Savva, Fisher Yu, Hao Su, Asako Kanezaki, Takahiko Furuya, Ryutarou Ohbuchi, Zhichao Zhou, Rui Yu, Song Bai, Xiang Bai, et al. Large-scale 3d shape retrieval from shapenet core55: Shrec'17 track. In *Eurographics Workshop on 3D Object Retrieval*, 2017.

J. Schmelzle, A. Lucchi, T. Kacprzak, A. Amara, R. Sgier, A. Réfrégier, and T. Hofmann. Cosmological model discrimination with deep learning. *arxiv:1707.05167*, 2017.

Yu-Chuan Su and Kristen Grauman. Learning spherical convolution for fast features from 360 imagery. In *Advances in Neural Information Processing Systems*, 2017.

SUPPLEMENTARY MATERIAL

A PROOF OF THEOREM 3.1

Preliminaries. The proof of theorem 3.1 is inspired from the work of Belkin & Niyogi (2008). As a result, we start by restating some of their results. Given a sampling $\mathcal{V} = \{x_i \in \mathcal{M}\}_{i=0}^{n-1}$ of a closed, compact and infinitely differentiable manifold $\mathcal{M}$, a smooth ($\in \mathcal{C}_\infty(\mathcal{M})$) function $f : \mathcal{M} \to \mathbb{R}$, and defined the vector $\boldsymbol{f}$ of samples of f as follows: $T_\mathcal{V} f = \boldsymbol{f} \in \mathbb{R}^n$, $\boldsymbol{f}_i = f(x_i)$. The proof is constructed by leveraging 3 different operators:

- The extended graph Laplacian operator is a linear operator $L_n^t : L^2(\mathcal{M}) \to L^2(\mathcal{M})$ is defined as
$$L_n^t f(y) := \frac{1}{n} \sum_{i=0}^{n-1} e^{-\frac{\|x_i - y\|^2}{4t}} \left(f(y) - f(x_i)\right). \tag{7}$$
Note that we have the following relation $\boldsymbol{L}_n^t \boldsymbol{f} = T_\mathcal{V} L_n^t f$.
- The functional approximation to the Laplace-Beltrami operator is a linear operator $L^t : L^2(\mathcal{M}) \to L^2(\mathcal{M})$ defined as
$$L^t f(y) = \int_\mathcal{M} e^{-\frac{\|x-y\|^2}{4t}} \left(f(y) - f(x)\right) d\mu(x), \tag{8}$$
where μ is the uniform probability measure on the manifold $\mathcal{M}$, and $\text{vol}(\mathcal{M})$ is the volume of $\mathcal{M}$.
- The Laplace-Beltrami operator $\Delta_\mathcal{M}$ is defined as the divergence of the gradient
$$\Delta_\mathcal{M} f(y) := -\text{div}(\nabla_\mathcal{M} f) \tag{9}$$
of a differentiable function $f : \mathcal{M} \to \mathbb{R}$. The gradient $\nabla f : \mathcal{M} \to T_p\mathcal{M}$ is a vector field defined on the manifold pointing towards the direction of steepest ascent of f, where $T_p\mathcal{M}$ is the affine space of all vectors tangent to $\mathcal{M}$ at p.

Leveraging these three operators Belkin & Niyogi (2008; 2007) have build proofs of both pointwise and spectral convergence of the extended graph Laplacian towards the Laplace-Beltrami operator in the general setting of any compact, closed and infinitely differentiable maniform $\mathcal{M}$, where the sampling scheme $\mathcal{V}$ is drawn randomly on the manifold. For this reason, their results are all to be interpreted in a probabilistic sense. Their proofs consist in establishing that (7) converges in probability towards (8) as $n \to \infty$ and (8) converges toward (9) as $t \to 0$. In particular, this second step is given by the following:

Proposition 1 (Belkin & Niyogi (2008), Proposition 4.4)**.** *Let $\mathcal{M}$ be a k-dimensional compact smooth manifold embedded in some Euclidean space $\mathbb{R}^N$, and fix $y \in \mathcal{M}$. Let $f \in \mathcal{C}_\infty(\mathcal{M})$. Then*

$$\frac{1}{t} \frac{1}{(4\pi t)^{k/2}} L^t f(y) \xrightarrow{t \to 0} \frac{1}{vol(\mathcal{M})} \Delta_\mathcal{M} f(y). \tag{10}$$

Building the proof. As the sphere is a compact smooth manifold embedded in $\mathbb{R}^3$, we can reuse proposition 1. Thus, our strategy to prove Theorem 3.1 is to a) show that

$$\lim_{n \to \infty} L_n^t f(y) = L^t(y) \tag{11}$$

for a particular class of *deterministic* sampling schemes and b) apply Proposition 1.

We start by proving that for smooth functions, for any fixed t, the extended graph Laplacian L_n^t converges towards its continuous counterpart L^t as the sampling increases in size.

Proposition 2. *For an equal area sampling $\{x_i \in \mathbb{S}^2\}_{i=0}^{n-1} : A_i = A_j \forall i, j$ of the sphere it is true that for all $f : \mathbb{S}^2 \to \mathbb{R}$ Lipschitz with respect to the Euclidean distance $\|\cdot\|$ with Lipschitz constant C_f*

$$\left| \int_{\mathbb{S}^2} f(x) d\mu(x) - \frac{1}{n} \sum_i f(x_i) \right| \leq C_f d^{(n)}.$$

Furthermore, for all $y \in \mathbb{S}^2$ the Heat Kernel Graph Laplacian operator L_n^t converges pointwise to the functional approximation of the Laplace Beltrami operator L^t

$$L_n^t f(y) \xrightarrow{n\to\infty} L^t f(y).$$

Proof. Assuming $f : \mathbb{S}^2 \to \mathbb{R}$ is Lipschitz with Lipschitz constant C_f, we have

$$\left| \int_{\sigma_i} f(x) \mathrm{d}\mu(x) - \frac{1}{n} f(x_i) \right| \leq C_f d^{(n)} \frac{1}{n},$$

where $\sigma_i \subset \mathbb{S}^2$ is the subset of the sphere corresponding to the patch arround x_i. Remember that the sampling is equal area. Hence, using the triangular inequality and summing all the contributions of the n patches, we obtain

$$\left| \int_{\mathbb{S}^2} f(x) \mathrm{d}\mu(x) - \frac{1}{n} \sum_i f(x_i) \right| \leq \sum_i \left| \frac{1}{4\pi^2} \int_{\sigma_i} f(x) \mathrm{d}\mu(x) - \frac{1}{n} f(x_i) \right| \leq n C_f d^{(n)} \frac{1}{n} = C_f d^{(n)}$$

A direct application of this result leads to the following pointwise convergences

$$\forall f \text{ Lipschiz}, \quad \forall y \in \mathbb{S}^2, \qquad \frac{1}{n} \sum_i e^{-\frac{\|x_i - y\|^2}{4t}} \to \int e^{-\frac{\|x-y\|^2}{4t}} d\mu(x)$$

$$\forall f \text{ Lipschiz}, \quad \forall y \in \mathbb{S}^2, \qquad \frac{1}{n} \sum_i e^{-\frac{||x_i - y||^2}{4t}} f(x_i) \to \int e^{-\frac{\|x-y\|^2}{4t}} f(x) d\mu(x)$$

Definitions 7 and 8 end the proof. □

The last proposition show that for a *fixed* t, $L_n^t f(x) \to 1/4\pi^2 L^t f(x)$. To utilize Proposition 1 and complete the proof, we need to find a sequence of t_n for which this holds as $t_n \to 0$. Furthermore this should hold with a faster decay than $\frac{1}{4\pi t_n^2}$.

Proposition 3. *Given a sampling regular enough, i.e., for which we assume $A_i = A_j \ \forall i, j$ and $d^{(n)} \leq \frac{C}{n^\alpha}$, $\alpha \in (0, 1/2]$, a Lipschitz function f and a point $y \in \mathbb{S}^2$ there exists a sequence $t_n = n^\beta, \beta < 0$ such that*

$$\forall f \textit{ Lipschitz}, \forall x \in \mathbb{S}^2 \quad \left| \frac{1}{4\pi t_n^2} \left(L_n^{t_n} f(x) - L^{t_n} f(x) \right) \right| \xrightarrow{n\to\infty} 0.$$

Proof. To ease the notation, we define

$$K^t(x, y) := e^{-\frac{\|x-y\|^2}{4t}} \tag{12}$$

$$\phi^t(x; y) := e^{-\frac{\|x-y\|^2}{4t}} \left(f(y) - f(x) \right). \tag{13}$$

We start with the following inequality

$$\begin{aligned}
\|L_n^t f - L^t f\|_\infty &= \max_{y \in \mathbb{S}^2} \left| L_n^t f(y) - L^t f(y) \right| \\
&= \max_{y \in \mathbb{S}^2} \left| \frac{1}{n} \sum_{i=1}^n \phi^t(x_i; y) - \int_{\mathbb{S}^2} \phi^t(x; y) d\mu(x) \right| \\
&\leq \max_{y \in \mathbb{S}^2} \sum_{i=1}^n \left| \frac{1}{n} \phi^t(x_i; y) - \int_{\sigma_i} \phi^t(x; y) d\mu(x) \right| \\
&\leq d^{(n)} \max_{y \in \mathbb{S}^2} C_{\phi_y^t},
\end{aligned} \tag{14}$$

where $C_{\phi_y^t}$ is the Lipschitz constant of $x \to \phi^t(x, y)$ and the last inequality follows from Proposition 2. Using the assumption $d^{(n)} \leq \frac{C}{\sqrt{n}}$ we find

$$\|L_n^t f - L^t f\|_\infty \leq \frac{C}{\sqrt{n}} \max_{y \in \mathbb{S}^2} C_{\phi_y^t}$$

We now find the explicit dependence between t and $C_{\phi_y^t}$

$$\begin{aligned}
C_{\phi_y^t} &= \|\partial_x \phi^t(\cdot; y)|_- \infty \\
&= \|\partial_x \left(K^t(\cdot; y) f\right)\|_\infty \\
&= \|\partial_x K^t(\cdot; y) f + K^t(\cdot; y) \partial_x f||_\infty \\
&\leq \|\partial_x K^t(\cdot; y) f\|_\infty + \|K^t(\cdot; y) \partial_x f\|_\infty \\
&\leq \|\partial_x K^t(\cdot; y)\|_\infty \|f\|_\infty + \|K^t(\cdot; y)\|_\infty \|\partial_x f\|_\infty \\
&= \|\partial_x K^t(\cdot; y)\|_\infty \|f\|_\infty + \|\partial_x f\|_\infty \\
&= C_{K_y^t} \|f\|_\infty + \|\partial_x f\|_\infty \\
&= C_{K_y^t} \|f\|_\infty + C_f
\end{aligned}$$

where $C_{K_y^t}$ is the Lipschitz constant of the function $x \to K^t(x; y)$. We note that this constant does not depend on y:

$$C_{K_y^t} = \left\| \partial_x e^{-\frac{x^2}{4t}} \right\|_\infty = \left\| \frac{x}{2t} e^{-\frac{x^2}{4t}} \right\|_\infty = \left. \frac{x}{2t} e^{-\frac{x^2}{4t}} \right|_{x=\sqrt{2t}} = (2et)^{-\frac{1}{2}} \propto t^{-\frac{1}{2}}.$$

Hence we have

$$\begin{aligned}
\frac{C}{\sqrt{n}} \max_{y \in \mathbb{S}^2} C_{\phi_y^t} &\leq \frac{C}{\sqrt{n}} \left((2et)^{-\frac{1}{2}} \|f\|_\infty + C_f \right) \\
&\leq \frac{C \|f\|_\infty}{n^\alpha (2et)^{1/2}} + \frac{C}{n^\alpha} C_f.
\end{aligned}$$

Inculding this result in (14) and rescaling by $1/4\pi t^2$, we obtain

$$\begin{aligned}
\left\| \frac{1}{4\pi t^2} \left(L_n^t f - L^t f \right) \right\|_\infty &\leq \frac{1}{4\pi t^2} \left\| \left(L_n^t f - L^t f \right) \right\|_\infty \\
&\leq \frac{C}{4\pi} \left[\frac{\|f\|_\infty}{\sqrt{2e}} \frac{1}{n^\alpha t^{5/2}} + \frac{C_f}{n^\alpha t^2} \right].
\end{aligned}$$

In order for $\frac{C}{4\pi} \left[\frac{\|f\|_\infty}{\sqrt{2e}} \frac{1}{n^\alpha t^{5/2}} + \frac{C_f}{n^\alpha t^2} \right] \xrightarrow[t \to 0]{n \to \infty} 0$, we need $\begin{cases} n^\alpha t^{5/2} \to \infty \\ n^\alpha t^2 \to \infty \end{cases}$

It happens if $\begin{cases} t(n) = n^\beta, & \beta \in (-\frac{2\alpha}{5}, 0) \\ t(n) = n^\beta, & \beta \in (-\frac{\alpha}{2}, 0) \end{cases} \implies t(n) = n^\beta, \quad \beta \in (-\frac{2\alpha}{5}, 0).$

Indeed, we have

$n^\alpha t^{5/2} = n^{5/2\beta + \alpha} \xrightarrow{n \to \infty} \infty$ since $\frac{5}{2}\beta + \alpha > 0 \iff \beta > -\frac{2\alpha}{5}$

and $n^\alpha t^2 = n^{2\beta + \alpha} \xrightarrow{n \to \infty} \infty$ since $2\beta + \alpha > 0 \iff \beta > -\frac{\alpha}{2}$.

As a result, for $t = n^\beta$ with $\beta \in (-\frac{1}{5}, 0)$ we have $\begin{cases} (t_n) \xrightarrow{n \to \infty} 0 \\ \left\| \frac{1}{4\pi t_n^2} L_n^{t_n} f - \frac{1}{4\pi t_n^2} L^{t_n} f \right\|_\infty \xrightarrow{n \to \infty} 0, \end{cases}$

which concludes the proof. □

Theorem 3.1, is then an immediate consequence of Proposition 3 and 1.

Proof of Theorem 3.1. Thanks to Proposition 3 and Proposition 1 we conclude that $\forall y \in \mathbb{S}^2$

$$\lim_{n \to \infty} \frac{1}{4\pi t_n^2} L_n^{t_n} f(y) = \lim_{n \to \infty} \frac{1}{4\pi t_n^2} L^{t_n} f(y) = \frac{1}{|\mathbb{S}^2|} \triangle_{\mathbb{S}^2} f(y)$$

Eventually selecting y as a point of the sampling, we obtain

$$\lim_{n \to \infty} \frac{|\mathbb{S}^2|}{4\pi t_n^2} \boldsymbol{L}_n^{t_n} T_{\mathcal{V}} f[i] = \Delta_{\mathbb{S}^2} f(x_i) \quad \forall i = 0, ..., n-1.$$

□

	micro (label average)				macro (instance average)			
	P@N	R@N	F1@N	mAP	P@N	R@N	F1@N	mAP
Cohen et al. (2018) ($b = 128$)	0.701	0.711	0.699	0.676	-	-	-	-
Cohen et al. (2018) (simplified, $b = 64$)	0.704	0.701	0.696	0.665	0.430	0.480	0.429	0.385
Esteves et al. (2018) ($b = 64$)	0.717	0.737	-	0.685	0.450	0.550	-	0.444
DeepSphere (equiangular $b = 64$)	0.709	0.700	0.698	0.665	0.439	0.489	0.439	0.403
DeepSphere (HEALPix $N_{side} = 32$)	0.725	0.717	0.715	0.686	0.475	0.508	0.468	0.428

Table 5: Official metrics from the SHREC'17 object retrieval competition.

In the work of Belkin & Niyogi (2008) the sampling is drawn form a uniform random distribution on the sphere, and their proof heavily relies on the uniformity properties of the distribution from which the sampling is drawn. In our case the sampling is deterministic, and this is indeed a problem that we need to overcome by imposing the regularity conditions above.

To conclude, we see that the result obtained is of similar form than the result obtained in Belkin & Niyogi (2008). Given the kernel density $t(n) = n^\beta$, Belkin & Niyogi (2008) proved convergence in the random case for $\beta \in (-\frac{1}{4}, 0)$ and we proved convergence in the deterministic case for $\beta \in (-\frac{2\alpha}{5}, 0)$, where $\alpha \in (0, 1/2]$ (for the spherical Manifold).

B Experimental details

B.1 3D objects recognition

Table 5 shows the results obtained from the competition's official evaluation script.

$$\begin{aligned}&[GC_{16} + BN + ReLU]_{nside32} + \text{Pool} + [GC_{32} + BN + ReLU]_{nside16} + \text{Pool}\\ &+ [GC_{64} + BN + ReLU]_{nside8} + \text{Pool} + [GC_{128} + BN + ReLU]_{nside4}\\ &+ \text{Pool} + [GC_{256} + BN + ReLU]_{nside2} + \text{Pool} + GAP + FCN + \text{softmax}\end{aligned} \tag{15}$$

B.2 Cosmological model classification

$$\begin{aligned}&[GC_{16} + BN + ReLU]_{nside1024} + \text{Pool} + [GC_{32} + BN + ReLU]_{nside512}\\ &+ \text{Pool} + [GC_{64} + BN + ReLU]_{nside256} + \text{Pool}\\ &+ [GC_{64} + BN + ReLU]_{nside128} + \text{Pool} + [GC_{64} + BN + ReLU]_{nside64}\\ &+ \text{Pool} + [GC_2]_{nside32} + GAP + \text{softmax}\end{aligned} \tag{16}$$

B.3 Climate event segmentation

Table 6, 7, and 8 show the accuracy, mAP, and efficiency of all the NNs we ran.

The experiment with the model from Jiang et al. (2019) was rerun in order to obtain the AP metrics, but with a batch size of 64 instead of 256 due to GPU memory limit.

Several experiments were run with different architectures for DeepSphere (DS). Jiang architecture use a similar one as Jiang et al. (2019), with only the convolutional operators replaced. DeepSphere only is the original architecture giving the best results, deeper and with four times more feature maps than Jiang architecture. And the wider architecture is the same as the previous one with two times the number of feature maps.

Regarding the weighted loss, the weights are chosen with `scikit-learn` function `compute_class_weight` on the training set.

	TC	AR	BG	mean
Mudigonda et al. (2017)	74	65	97	78.67
Jiang et al. (2019) (paper)	94	93	97	94.67
Jiang et al. (2019) (rerun)	93.9	95.7	95.2	94.95
Cohen et al. (2019) (S2R)	97.8	97.3	97.3	97.5
Cohen et al. (2019) (R2R)	97.9	97.8	97.4	97.7
DS (Jiang architecture, weighted loss)	97.1	97.6	96.5	97.1
DS (weighted loss)	97.4 ± 1.1	97.7 ± 0.7	98.2 ± 0.5	97.8 ± 0.3
DS (wider architecture, weighted loss)	91.5	93.4	99.0	94.6
DS (Jiang architecture, non-weighted loss)	33.6	93.6	99.3	75.5
DS (non-weighted loss)	69.2 ± 3.7	94.5 ± 2.9	99.7 ± 0.1	87.8 ± 0.5
DS (wider architecture, non-weighted loss)	73.4	92.7	99.8	88.7

Table 6: Results on climate event segmentation: accuracy. Tropical cyclones (TC) and atmospheric rivers (AR) are the two positive classes, against the background (BG). Mudigonda et al. (2017) is not directly comparable as they don't use the same input feature maps. Note that a non-weighted cross-entropy loss is not optimal for the accuracy metric.

	TC	AR	mean
Jiang et al. (2019) (rerun)	11.08	65.21	38.41
Cohen et al. (2019) (S2R)	-	-	68.6
Cohen et al. (2019) (R2R)	-	-	75.9
DS (Jiang architecture, non-weighted loss)	46.2	93.9	70.0
DS (non-weighted loss)	80.86 ± 2.42	97.45 ± 0.38	89.16 ± 1.37
DS (wider architecture, non-weighted loss)	84.71	98.05	91.38
DS (Jiang architecture, weighted loss)	49.7	89.2	69.5
DS (weighted loss)	58.88 ± 3.17	95.41 ± 1.51	77.15 ± 1.94
DS (wider architecture, weighted loss)	52.80	94.78	73.79

Table 7: Results on climate event segmentation: average precision. Tropical cyclones (TC) and atmospheric rivers (AR) are the two positive classes. Note that a weighted cross-entropy loss is not optimal for the average precision metric.

	size	speed	
	params	inference	training
Jiang et al. (2019)	330 k	10 ms	10 h
DeepSphere (Jiang architecture)	590 k	5 ms	3 h
DeepSphere	13 M	33 ms	13 h
DeepSphere (wider architecture)	52 M	50 ms	20 h

Table 8: Results on climate event segmentation: size and speed.

DeepSphere with Jiang architecture
encoder:

$$\begin{aligned}&[GC_8 + BN + ReLU]_{L5} + \text{Pool} + [GC_{16} + BN + ReLU]_{L4} + \text{Pool}\\&+ [GC_{32} + BN + ReLU]_{L3} + \text{Pool} + [GC_{64} + BN + ReLU]_{L2} + \text{Pool}\\&+ [GC_{128} + BN + ReLU]_{L1} + \text{Pool} + [GC_{128} + BN + ReLU]_{L0}\end{aligned} \tag{17}$$

decoder:

$$\begin{aligned}&\text{Unpool} + [GC_{128} + BN + ReLU]_{L1} + \text{concat} + [GC_{128} + BN + ReLU]_{L1}\\&+ \text{Unpool} + [GC_{64} + BN + ReLU]_{L2} + \text{concat}\\&+ [GC_{64} + BN + ReLU]_{L2} + \text{Unpool} + [GC_{32} + BN + ReLU]_{L3}\\&+ \text{concat} + [GC_{32} + BN + ReLU]_{L3} + \text{Unpool}\\&+ [GC_{16} + BN + ReLU]_{L4} + \text{concat} + [GC_{16} + BN + ReLU]_{L4} + \text{Unpool}\\&+ [GC_8 + BN + ReLU]_{L5} + \text{concat} + [GC_8 + BN + ReLU]_{L5} + [GC_3]_{L5}\end{aligned} \tag{18}$$

Concat is the operation that concatenate the results of the corresponding encoder layer.

Original DeepSphere architecture with encoder decoder
encoder:

$$\begin{aligned}&[GC_{32} + BN + ReLU]_{L5} + [GC_{64} + BN + ReLU]_{L5}\\&+ \text{Pool} + [GC_{128} + BN + ReLU]_{L4} + \text{Pool}\\&+ [GC_{256} + BN + ReLU]_{L3} + \text{Pool} + [GC_{512} + BN + ReLU]_{L2}\\&+ \text{Pool} + [GC_{512} + BN + ReLU]_{L1} + \text{Pool} + [GC_{512}]_{L0}\end{aligned} \tag{19}$$

decoder:

$$\begin{aligned}&\text{Unpool} + [GC_{512} + BN + ReLU]_{L1} + \text{concat} + [GC_{512} + BN + ReLU]_{L1}\\&+ \text{Unpool} + [GC_{256} + BN + ReLU]_{L2} + \text{concat}\\&+ [GC_{256} + BN + ReLU]_{L2} + \text{Unpool} + [GC_{128} + BN + ReLU]_{L3}\\&+ \text{concat} + [GC_{128} + BN + ReLU]_{L3} + \text{Unpool}\\&+ [GC_{64} + BN + ReLU]_{L4} + \text{concat} + [GC_{64} + BN + ReLU]_{L4}\\&+ \text{Unpool} + [GC_{32} + BN + ReLU]_{L5} + [GC_3]_{L5}\end{aligned} \tag{20}$$

B.4 UNEVEN SAMPLING

Architecture for dense regression:

$$[GC_{50} + BN + ReLU] + [GC_{100} + BN + ReLU] + [GC_{100} + BN + ReLU] + [GC_1] \tag{21}$$

Architecture for global regression:

$$\begin{aligned}&[GC_{50} + BN + ReLU] + [GC_{100} + BN + ReLU]\\&+ [GC_{100} + BN + ReLU] + GAP + FCN\end{aligned} \tag{22}$$